Advances in experimental mechanics by the synergetic combination of full-field measurement techniques and computational tools ☆

Gabriella Bolzon *

Politecnico di Milano, Department of Civil and Environmental Engineering, Piazza Leonardo da Vinci 32, 20133 Milano, Italy

Article history:
Received 23 January 2014
Received in revised form 21 March 2014
Accepted 18 April 2014
Available online 2 May 2014

1. Introduction

The continuous improvement of full-field measurement techniques has fostered the development of mechanical testing procedures of increasing complexity, which can be performed at smaller and smaller scales [1–7], on heterogeneous material samples [8–10] and in non-destructive manner even on final components [11–13]. Contemporarily, the design of the experiments and the interpretation of the acquired data benefit of the realism of available numerical models while several computing tools of enhanced effectiveness permit to alleviate the large burden usually associated to the repetitive simulation of the testing procedures [14–26]. Thus, non-linear phenomena like large inelastic deformation, damage and fracture can be accounted for, for instance in indirect parameter calibration techniques developed to provide results in almost real time for routine use in industrial environment [12,16,25].

This contribution summarizes some recent experiences relevant to the synergetic coupling of the above mentioned experimental and computational tools exploited to either model calibration or model verification purposes in materials mechanics context. The possibilities at present offered by computational tools to the effective exploitation of information returned by advanced experimental techniques are illustrated.

2. Methods

Digital image correlation (DIC) methods are commonly employed in the monitoring of plane structural components, not only to replace conventional measurement devices like strain gages and LVDTs (linear voltage differential transformers) [7,13,27] but also to recover the whole strain and displacement field within the monitored regions [4,6,8–14,27–31] with assessed metrology performances [32]. The development and use of three-dimensional (3D) DIC techniques are also in progress [33–35] and come up

---

☆ An extract from this contribution has been presented in oral form at the 30th Danubia–Adria Symposium on Advances in Experimental Mechanics.

* Tel.: +39 022399 4319; fax: +39 022399 4300.
E-mail address: gabriella.bolzon@polimi.it

beside more traditional approaches like microscopy and profilometry for the determination of out-of-plane displacement components [1,2,5,12,36].

These pieces of information may constitute the input of inverse analysis procedures more and more often exploited to material characterization and structural diagnostic purposes, which involve the minimization of the discrepancy between the available measurements and the output of the simulated experiments [37].

In this context, most details (for instance, the specimen or component geometry and size) are fixed and the system response depends on a few parameters (say z_k, gathered in vector $\mathbf{z}$) representing for instance the material properties. Let u_{mi} (subscript m) represent N_h collected measurements and let u_{ci} (subscript c) be the corresponding quantities obtained from a simulation model of the test, depending on the input $\mathbf{z}$. The actual z_k values can be estimated by the minimization of the discrepancy function $\omega(\mathbf{z})$, which can be defined in a least square sense, for instance as follows:

$$\omega(\mathbf{z}) = \frac{1}{N_u}\sum_{i=1}^{N_u}\left(\frac{u_{mi} - u_{ci}(\mathbf{z})}{u_{\max}}\right)^2 \tag{1}$$

In the above expression, $u_{\max}$ represents a normalization coefficient, which renders $\omega(\mathbf{z})$ dimensionless. This factor can be replaced by the entries of a positive definite symmetric weighting matrix related to the statistical characterization of measurement errors [37].

The minimization problem can be approached by different solution techniques, for instance by first order iterative algorithms or by zero-th order evolutive (e.g. genetic) search procedures available in popular optimization tools [38]. Both techniques require to evaluate the system response and, possibly, its derivatives with respect to the z_k parameters numerous times, varying the input values. Computations are rather heavy when non-linear phenomena are involved and analyses are performed by finite element (FE) approaches.

However, an analytical approximation of the system response can be always recovered: defining an a priori established number of input combinations in the sought parameter space; evaluating the system response in these knot points by accurate simulation methods; interpolating these preliminary results in order to generalize the solution to different input data sets.

This methodology can be optimized ensuring adequate accuracy, keeping the control over the numerical efforts by an appropriate selection of the interpolation function.

A common approach is based on Lagrange polynomials defined over a regular grid of knot points; see e.g. [25] and references therein. The expected correlation of the system response for the selected z_k input values allows the analytical approximation to be fairly accurate with relatively low polynomial order. Nonetheless, the number of direct analyses to be performed increases rapidly with the number of unknowns and with the selected polynomial order. Moreover, the admissible parameter space to be investigated is not necessarily box-shaped [18,36].

The above limitations can be circumvented by the use of radial basis functions (RBFs) [39], which represent a rather flexible tool since the RBF formulation can be selected on the basis of the specific application. RBFs are for instance often employed in 3D computer graphics reconstructions [40].

The accuracy of the overall procedure can be improved by the reduction of noises associated either to the experimental input or to the simulation models. This goal can be achieved by the consideration of data compression schemes, for instance based on proper orthogonal decomposition (POD), or principal component analysis. Besides drastically reducing computing times and costs, this provision permits to retain the essential features of the considered system response and to filter most disturbances [22–24].

The POD operative procedure applied to a simulation model consists of the following steps:

i. An initial set of admissible parameter combinations $\bar{\mathbf{z}}_i$ is generated within the region of interest. Vectors $\bar{\mathbf{z}}_i$ are collected by the training matrix $\bar{\mathbf{Z}}$.
ii. Each knot vector $\bar{\mathbf{z}}_i$ defines one input parameter set for the numerical (FE) analysis, which returns the corresponding system response, named *snapshot* in the present context. Snapshots are stored in matrix $\mathbf{U}$ in ordered correspondence with the vectors stored in matrix $\bar{\mathbf{Z}}$.
iii. Eigen-pairs of the matrix $\mathbf{D} = \mathbf{U}^{\mathrm{T}} \cdot \mathbf{U}$ are computed in a sequence, starting from the largest eigenvalue and truncating the search as the returned value is smaller than some established threshold. In fact, due to the expected correlation of the information stored in matrix $\mathbf{U}$, a large number of zero or nearly null eigenvalues is expected. The retained eigenvectors associated to matrix $\mathbf{D}$ represent response modes stored in matrix $\mathbf{V}$, while the square root of the inverse of the eigenvalues define the diagonal matrix $\mathbf{\Lambda}^{-1/2}$.
iv. The retained eigen–pairs permit to build up the matrix $\mathbf{\Phi} = \mathbf{U} \cdot \mathbf{V} \cdot \mathbf{\Lambda}^{-1/2}$ (such that $\mathbf{\Phi}^{\mathrm{T}} = \mathbf{\Phi}^{-1}$), which represents an optimally truncated orthonormal reference system for reconstructing the system response.
v. Snapshot data are approximated by the linear combination $\mathbf{U} = \mathbf{\Phi} \cdot \mathbf{A}$, where matrix $\mathbf{A} = \mathbf{\Phi}^{\mathrm{T}} \cdot \mathbf{U}$ collects the amplitudes of the new basis combination.

Thus, the system response corresponding to each parameter vector $\bar{\mathbf{z}}$ is represented by a number of coefficients stored in the amplitude matrix $\mathbf{A}$, with an approximation that depends on the number of retained modes and on the informative content of the neglected ones, roughly quantified by the sum of the discarded eigenvalues compared to the larger ones [24].

Truncation is however beneficial in the case of noisy results, represented for instance in the graph of Fig. 1, which corresponds to the output of a simulated indentation experiment. Details on the mechanical problem and on its numerical model are provided in [18]. The oscillations shown by the FE simulation are produced by the enforcement of frictional contact conditions over a relatively coarse mesh made of solid elements. This

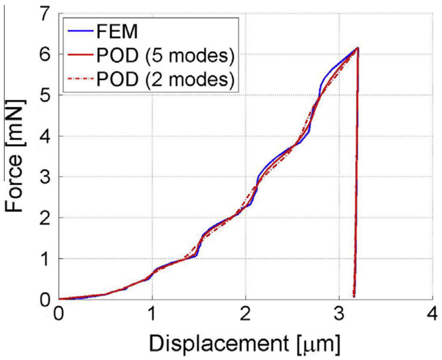

Fig. 1. The filtering capabilities of POD–RBF approximations based on 2 and 5 retained modes of a noisy FE simulation.

numerical inconvenient is almost completely eliminated by the corresponding POD approximation, which captures the main characteristics of the system response with only two retained modes. The fast initial decay of the eigenvalues associated to this simulation problem can be appreciated from Table 1, which reports the first six larger figures.

POD filtering capability increases the accuracy of derivatives estimated from the computational responses, which enter the minimization procedure of the discrepancy function (1), and regularizes the interpolation of large amounts of experimentally acquired data that can be used in conjunction with or in alternative to the simulation output [24]. In fact, the above introduced representation v. can be extended to the response $\mathbf{u}(\mathbf{z})$, corresponding to the generic parameter set $\mathbf{z}$ defined within the region of interest and not included in the initial selection $\bar{\mathbf{z}}$, assuming that:

$$\mathbf{u}(\mathbf{z}) = \mathbf{\Phi} \cdot \mathbf{a}(\mathbf{z}) \qquad (2)$$

where the vector valued function $\mathbf{a}(\mathbf{z})$ results from a suitable (RBF in this context) interpolation of the coefficients stored in the amplitude matrix $\mathbf{A}$.

3. Selected applications

The combination of full-field measurement and simulation techniques to model calibration and model validation purposes is illustrated in this section concerning the reconstruction of 3D deformation states by microscopy and profilometry methods. The reciprocal advantages arising from the coupling of complementary experimental and computational investigation tools are thus highlighted.

3.1. Model calibration

Instrumented indentation is often exploited to recover the mechanical characteristics of structural materials especially at the micron scale, where alternative testing procedures are seldom applicable [1,3,5]. Information is usually collected from the curves that visualize the relation between the penetration of the indenter tip and the applied force. Microscopy images of the imprint left on the sample surface can be acquired and are mainly used to examine plastic deformation mechanisms under load and to improve hardness measurements and elastic modulus estimation [41–44]. However, these geometrical data can be exploited to material characterization purposes to a much wider extent [45,46].

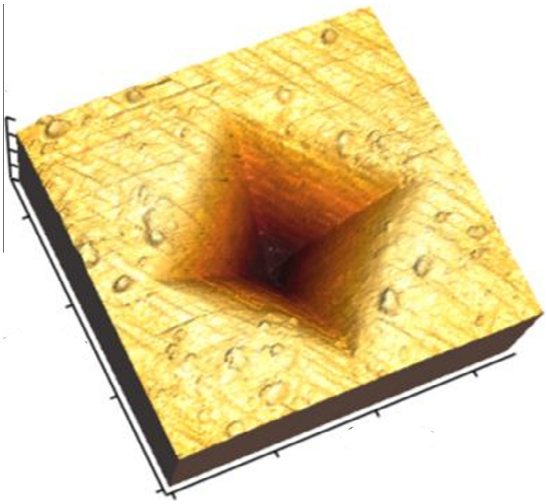

Fig. 2. AFM imaging of the imprint left by Vickers (pyramidal) indentation on the surface of a zirconia specimen.

Scanning capabilities at atomic force microscope (AFM) scale are more and more often integrated to indentation instruments. The high resolution micrographs obtained by AFM constitute an ideal input for DIC techniques since high contrast random patterns are naturally created on the specimen surface by the roughness, which acts as distributed markers [2,4,29,30].

As an example, Fig. 2 shows the AFM image of the geometry of the residual imprint left by Vickers (pyramidal) [47] micro-indentation on the surface of a zirconia sample for biomechanical applications [5]. This information can be exploited with the curves in Fig. 4 in order to characterize the mechanical behavior of this ceramic.

Indentation curves and imprint geometry reflect the sought mechanical properties in indirect manner. Therefore, the interpretation of the experimental records and the recovery of constitutive parameters benefit from identification procedures resting on the combination of the test with its simulation, performed in this case by a FE model implemented in a commercial code often used for similar purposes [48].

The computational burden can be controlled by the expected symmetries of the system response, considered

Table 1
Eigenvalue sequence in the POD of the indentation results represented in Fig. 1.

3.445E+05	2.654E+01	1.262E+01	3.249E+00	2.681E+00	1.458E+00

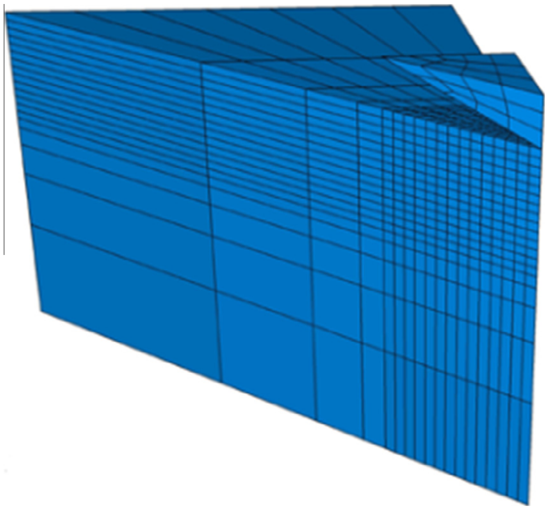

Fig. 3. FE model of Vickers indentation test.

in the FE mesh shown in Fig. 3. Still, the progressive enforcement of the contact conditions on the sample surface and the large inelastic strains developing under the indenter tip require to account for significant material and geometrical non-linearity. Thus, the analysis can greatly benefit from the model reduction provisions introduced in Section 2.

The mechanical response of zirconia can be described by an associative elastic–plastic constitutive law based on the classical Drucker–Prager criterion, a characteristic shared with metal-based composites with high ceramic content [26,49]. The main material properties entering this isotropic model consist of Young's modulus E and of the coefficients of function f defining the yield surface in the stress space:

$$f = \sqrt{\frac{1}{2}\sigma'_{ij}\sigma'_{ij}} + \alpha I_1 - k - h\lambda \tag{3}$$

In expression (3): σ'_{ij} denote the components of the deviatoric stress tensor; I_1 represents the first stress invariant; λ (>0) is the cumulative multiplier of the plastic deformations that develop beyond the elastic threshold; parameter h governs the assumed linear hardening while the internal friction angle α and the initial cohesion k depend on the initial tensile and compressive yield limits, σ_{0t} and σ_{0c} respectively, as follows:

$$\alpha = \sqrt{3}\frac{\sigma_{0c} - \sigma_{0t}}{\sigma_{0c} + \sigma_{0t}}, \quad k = \frac{2}{\sqrt{3}}\frac{\sigma_{0c}\sigma_{0t}}{\sigma_{0c} + \sigma_{0t}} \tag{4}$$

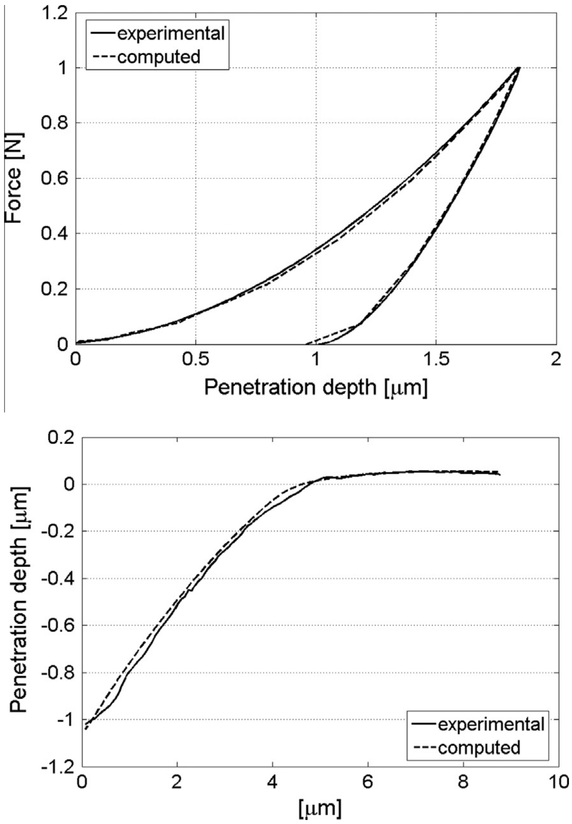

Fig. 4. Indentation curves and imprint mapping (diagonal profile): experimental data and recalculated results.

The simulation results are included in the discrepancy function (1), formulated in terms of the information relevant either to the indentation curve or to both the indentation curve and the geometry of the residual imprint. The material characteristics are recovered by an iterative gradient-based minimization technique, which leads to the parameter values summarized in Table 2. It is worth noticing that the consideration of the indentation curve only provides results that depend on the initialization values. On the contrary, the supplement of data relevant to the imprint improves the robustness of the procedure and the consequent reliability of the estimates, which differ of round-off amounts only.

The realism of the simulation model and the accuracy of the calibration procedure is evidenced by the graphs of Fig. 4, which visualize the gathered experimental

Table 2
Initial guess and final parameter estimates (bold values) recovered from the information represented in Figs. 2 and 4.

	Indentation curve				Indentation curve and imprint mapping			
	E (GPa)	σ_{0c} (MPa)	h (GPa)	α	E (GPa)	σ_{0c} (MPa)	h (GPa)	α
Initial guess	150	1,500	224,000	40	100	700	20,000	10
Final estimate	**201**	**1,995**	**155,410**	**19**	**209**	**2,715**	**39,638**	**32**
Initial guess	300	2,000	150,000	30	160	1,500	70,000	10
Final estimate	**211**	**991**	**145,214**	**27**	**209**	**2,713**	**39,660**	**32**
Initial guess	180	450	150,000	20	250	5,000	150,000	27
Final estimate	**193**	**481**	**103,120**	**30**	**210**	**2,716**	**39,533**	**32**

information and the corresponding numerical output, obtained with the most trusty values of the identified parameter set.

3.2. Model verification

The usefulness of full-field measurements to verification purposes increases with the availability of models, which describe the response of the systems under consideration. This is for instance the case of the mechanical behavior of paperboard, a key material in packaging industry, for which several constitutive laws of increasing complexity have been proposed, e.g. [50–53]. Still, the classical Hill's plasticity model [54,55] is often considered in this context for its relative simplicity and its capability of reproducing the main features of paperboard response, in particular the marked orthotropic characteristics induced by the industrial production processes.

The material is mainly used in foils in membrane stress conditions. Therefore, the relationship between the most meaningful strain and stress components can be referred to a local reference system coinciding with the in–plane material symmetry axes, here designated 1 and 2, and with the thickness direction 3.

The linear response in the elastic range can be represented by:

$$\begin{Bmatrix} \varepsilon_{11} \\ \varepsilon_{22} \\ \gamma_{12} \end{Bmatrix} = \begin{bmatrix} 1/E_1 & -\nu_{21}/E_2 & 0 \\ -\nu_{12}/E_1 & 1/E_2 & 0 \\ 0 & 0 & 1/G_{12} \end{bmatrix} \begin{Bmatrix} \sigma_{11} \\ \sigma_{22} \\ \sigma_{12} \end{Bmatrix} \tag{5}$$

where E_1, E_2, G_{12} and ν_{12} (or ν_{21}) can be assumed as independent material properties while the symmetry of the elastic tensor introduced with relation (5) requires that the ratio between the lateral contraction ratios ν_{21}/ν_{12} equals the ratio between the elastic moduli E_2/E_1.

The yield surface defined by Hill's criterion and its evolution under the hypothesis of isotropic exponential hardening can be described by the function:

$$f = \sqrt{\left(\frac{\sigma_{11}}{\sigma_{011}}\right)^2 + \left(\frac{\sigma_{22}}{\sigma_{022}}\right)^2 - \left(\frac{1}{\sigma_{011}^2} + \frac{1}{\sigma_{022}^2} - \frac{1}{\sigma_{033}^2}\right)\sigma_{11}\sigma_{22} + \left(\frac{\sigma_{12}}{\sigma_{012}}\right)^2} - \left(1 + \frac{\varepsilon_p}{\varepsilon_0}\right)^n \tag{6}$$

where σ_{011}, σ_{022} and σ_{033} represent the initial elastic limits along the main material directions and σ_{012} is the initial yield stress in shear. These parameters define the ellipsoidal shape of the elastic domain in the membrane plane while exponent n governs the size of this locus, which widens with the accumulated equivalent plastic strain ε_p [55]. Finally, the factor ε_0 represents a normalization term.

The model can be calibrated on the basis of the experimental information shown in Fig. 5, consisting of data collected from tensile tests performed on strips cut along different material directions according to Standards [56]. However, the value of parameter σ_{033} is difficult to be determined and is rather fixed on the basis of some a priori conjecture [57,58], also in view of the reduced sensitivity of the material response to the coefficient of the bilinear term $\sigma_{11}\sigma_{22}$ in relation (6) [36,59]. It is therefore desirable to verify the reliability of the model and of its calibrated parameters on the basis of the results of an independent experiment, which may consist of the inflation test performed by the prototype equipment shown in Fig. 6 [60].

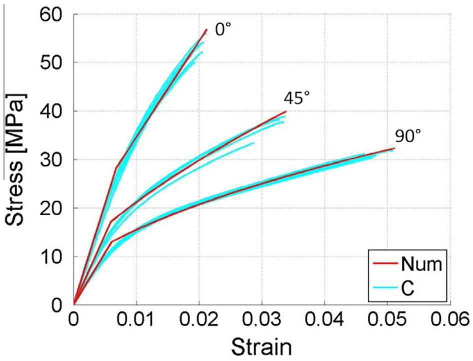

Fig. 5. Experimental results and calibrated stress–strain relationship of paperboard (material batch C).

The material sample to be tested is placed over a circular hole of 50 mm radius opened on the top of the cylindrical vessel visualised in the picture, filled with air at controlled pressure, temperature and humidity. The specimen is inserted between the stiff plates of an air-proof flange and fixed by bolts. The out-of-plane displacements of the inflated membrane are monitored by the rotating laser-blade of a profilometer connected with a computer, which records the measurements acquired at pre-fixed levels of pressure.

The graphical representation of a typical output is shown in Fig. 7, which evidences the position of the fixing bolts. These rough data are processed in order to transfer all information to an intrinsic reference system having two axes laying on a plane parallel to the initially flat membrane, easily individuated from the position of the plate supporting the flange, and the third one orthogonal to this reference plane.

The shape of the inflated foil can be used to assess the reliability of the calibrated material properties since all material directions contribute to the overall deformation of the specimen, which presents only slight deviations from the geometry of an isotropic solid. The simulation

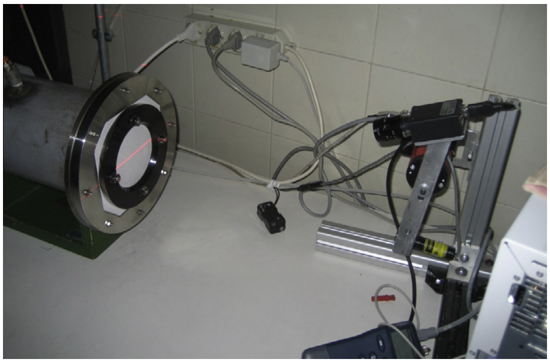

Fig. 6. Inflation test equipment.

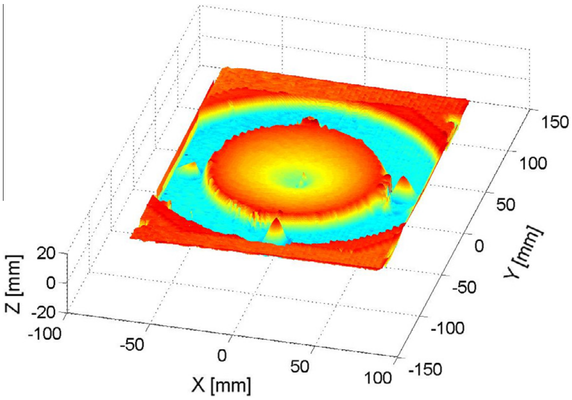

Fig. 7. Graphical output of an inflation test.

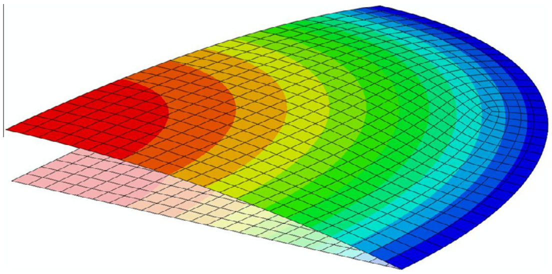

Fig. 8. FE simulation of an inflated orthotropic foil with paperboard properties.

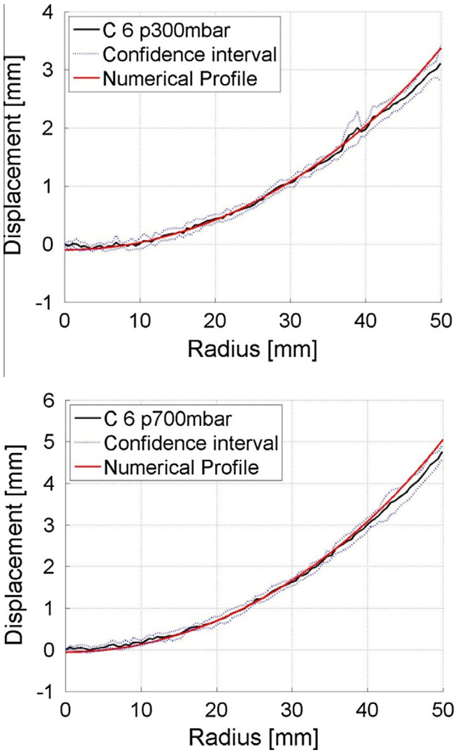

Fig. 9. Comparison between experimental and numerical results of the inflation test: the average profile of the inflated membrane under 300 mbar and 700 mbar (30 kPa and 70 kPa) pressure.

model shown in Fig. 8 has been used at the present purpose. The analysis is performed in a large displacement framework in order to overcome the otherwise hypostatic initial configuration of the foil. The satisfactory agreement between the mean experimental profile and the corresponding numerical result at different pressure levels is visualised in Fig. 9.

4. Closing remarks

Based on some recent experiences, it has been shown that the coupling of complementary investigation tools in experimental and computational mechanics fosters advances in both fields since:

- the design and the interpretation of the results of sophisticated testing procedures can be enhanced by the support of appropriate simulation tools;
- the realism of models describing physical phenomena can be improved and validated by full-field measurement techniques;
- the simulation of routine experiments can be performed in almost real time by model reduction provisions, leading e.g. to accurate POD–RBF approximations;
- model parameters like constitutive properties can be reliably and effectively identified even from fast and inexpensive non-destructive techniques.

References

[1] S.P. Baker, Between nanoindentation and scanning force microscopy: measuring mechanical properties in the nanometer regime, Thin Solid Films 308–309 (1997) 289–296.

[2] F.J. Giessibi, Advances in atomic force microscopy, Rev. Mod. Phys. 75 (2003) 949–983.

[3] S. Stauss, P. Schwaller, J.L. Bucaille, R. Rabe, L. Rohr, J. Michler, E. Blank, Determining the stress–strain behaviour of small devices by nanoindentation in combination with inverse methods, Microelectron. Eng. 67–68 (2003) 818–825.

[4] T.A. Berfield, J.K. Patel, R.G. Shimmin, P.V. Braun, J. Lambros, N.R. Sottos, Micro- and nanoscale deformation measurement of surface and internal planes via digital image correlation, Exp. Mech. 47 (2007) 51–62.

[5] G. Bolzon, M. Bocciarelli, E.J. Chiarullo, Mechanical characterization of materials by micro-indentation and AFM scanning, in: B. Bhushan, H. Fuchs (Eds.), Applied Scanning Probe Methods XII – Characterization, Springer, Berlin, 2008, pp. 85–120.

[6] G. Nicoletto, T. Marin, G. Anzelotti, R. Roncella, Application of high magnification digital image correlation technique to micromechanical strain analysis, Strain 47 (2011) e66–e73.

[7] J.-J. Lin, Y.-L. Wub, C.-F. Yang, W.-W. Wanga, Measurement of thermal expansion coefficient of INVAR foil using atomic force microscopy, Measurement 47 (2014) 373–378.

[8] A. Bernasconi, F. Cosmi, E. Zappa, Combined effect of notches and fibre orientation on fatigue behaviour of short fibre reinforced polyamide, Strain 46 (2010) 435–445.

[9] S.G. Shah, J.M. Chandra Kishen, Fracture properties of concrete–concrete interfaces using digital image correlation, Exp. Mech. 51 (2011) 303–313.

[10] G. Bolzon, V. Buljak, E. Zappa, Characterization of fracture properties of thin aluminum inclusions embedded in anisotropic laminate composites, Fratt. Integ. Strutt. 19 (2012) 20–28.

[11] R. Jiang, D.V. Jáuregui, K.R. White, Close-range photogrammetry applications in bridge measurement: literature review, Measurement 41 (2008) 823–834.

[12] G. Bolzon, B. Molinas, M. Talassi, Mechanical characterisation of metals by indentation tests: an experimental verification study for on-site applications, Strain 48 (2012) 517–527.

[13] B. Gencturk, K. Hossain, A. Kapadia, E. Labib, Y.-L. Mo, Use of digital image correlation technique in full-scale testing of prestressed concrete structures, Measurement 47 (2014) 505–515.

[14] S. Belhabib, H. Haddadi, M. Gaspérini, P. Vacher, Heterogeneous tensile test on elastoplastic metallic sheets: comparison between FEM simulations and full-field strain measurements, Int. J. Mech. Sci. 50 (2008) 14–21.

[15] S. Niroomandi, I. Alfaro, E. Cueto, F. Chinesta, Real-time deformable models of non–linear tissues by model reduction techniques, Comput. Methods Programs Biomed. 91 (2008) 223–231.

[16] G. Bolzon, V. Buljak, An effective computational tool for parametric studies and identification problems in materials mechanics, Comput. Mech. 48 (2011) 675–687.

[17] G. Bolzon, M. Talassi, Model reduction techniques in computational materials mechanics, in: G. Zavarise, D.P. Boso (Eds.), Bytes and Science, CIMNE, Barcelona, 2012, pp. 131–141.

[18] G. Bolzon, M. Talassi, An effective inverse analysis tool for parameter identification of anisotropic material models, Int. J. Mech. Sci. 77 (2013) 130–144.

[19] H.V. Ly, H.T. Tran, Modeling and control of physical processes using proper orthogonal decomposition, Math. Comput. Model. 33 (2001) 223–236.

[20] Y.C. Liang, H.P. Lee, S.P. Lim, W.Z. Lin, K.H Lee, C.G. Wu, Proper orthogonal decomposition and its applications – Part I: Theory, J. Sound Vib. 252 (2002) 527–544.

[21] C.M. Tiago, V.M.A. Leitão, Application of radial basis functions to linear and nonlinear structural analysis problems, Comput. Math. Appl. 51 (2006) 1311–1334.

[22] P. Druault, P. Guibert, F. Alizon, Use of proper orthogonal decomposition for time interpolation from PIV data. Application to the cycle-to-cycle variation analysis of in-cylinder engine flows, Exp. Fluids 39 (2005) 1009–1023.

[23] S. Deparis, G. Rozza, Reduced basis method for multi-parameter-dependent steady Navier–Stokes equations: applications to natural convection in a cavity, J. Comput. Phys. 228 (2009) 4359–4378.

[24] R. Gosh, Y. Joshi, Error estimation in POD-based dynamic reduced-order thermal modeling of data centers, Int. J. Heat Mass Transfer 57 (2013) 698–707.

[25] M. Bocciarelli, G. Bolzon, Indentation and imprint mapping for the identification of interface properties in film–substrate systems, Int. J. Fract. 155 (2009) 1–17.

[26] G. Bolzon, E.J. Chiarullo, P. Egizabal, C. Estournes, Constitutive modelling and mechanical characterization of aluminium-based metal matrix composites produced by spark plasma sintering, Mech. Mater. 42 (2010) 548–558.

[27] Y.H. Wang, J.H. Jiang, C. Wanintrudal, C. Du, D. Zhou, L.M. Smith, L.X. Yang, Whole field sheet–metal tensile test using digital image correlation, Exp. Tech. (2010) 54–59.

[28] S. Yoneyama, Y. Morimoto, M. Takashi, Automatic evaluation of mixed-mode stress intensity factors utilizing digital image correlation, Strain 42 (2006) 21–29.

[29] S.W. Cho, I. Chasiotis, Elastic properties and representative volume element of polycrystalline silicon for MEMS, Exp. Mech. 47 (2007) 37–49.

[30] W.A. Scrivens, Y. Luo, M.A. Sutton, S.A. Collette, M.L. Myrick, P. Miney, P.E. Colavita, A.P. Reynolds, X. Li, Development of patterns for digital image correlation measurements at reduced length scales, Exp. Mech. 47 (2007) 63–77.

[31] G. Zhang, Y. Hu, J.-M. Zhang, New image analysis-based displacement-measurement system for geotechnical centrifuge modeling tests, Measurement 42 (2009) 87–96.

[32] M. Bornert, F. Brémand, P. Doumalin, J.C. Dupré, M. Fazzini, M. Grédiac, F. Hild, S. Mistou, J. Molimard, J.J. Orteu, L. Robert, Y. Surrel, P. Vacher, B. Wattrisse, Assessment of digital image correlation measurement errors: methodology and results, Exp. Mech. 49 (2009) 353–370.

[33] O. De Almeida, F. Lagattu, J. Brillaud, Analysis by a 3D DIC technique of volumetric deformation gradients: application to polypropylene/EPR/talc composites, Composites A 39 (2008) 1210–1217.

[34] B. Pan, H. Xie, L. Yang, Z. Wang, Accurate measurement of satellite antenna surface using 3D digital image correlation technique, Strain 45 (2009) 194–200.

[35] M. Lopez-Pedrosa, M. Zanganeh, Y.H. Tai, C. Pinna, 3D digital image correlation (DIC) analysis in relation to damage development in third generation AA2050-T851 aluminium alloy, J. Phys.: Conf. Ser. 382 (2012) 012034.

[36] M. Ageno, G. Bolzon, G. Maier, An inverse analysis procedure for the material parameter identification of elastic–plastic free-standing foils, Struct. Multidisciplinary Optim. 38 (2009) 229–243.

[37] G. Stavroulakis, G. Bolzon, Z. Waszczyszyn, L. Ziemianski, Inverse analysis, in: B. Karihaloo, R.O. Ritchie, I. Milne (Eds.), Comprehensive Structural Integrity, Numerical and Computational Methods, vol. 3, Elsevier, Amsterdam, 2003, pp. 685–718.

[38] Matlab, User's Guide and Optimization Toolbox, release 7.4.0, The Math Works Inc., USA, 2007.

[39] M.D. Buhmann, Radial Basis Functions: Theory and Implementations, Cambridge University Press, 2003.

[40] J.C. Carr, R.K. Beatson, J.B. Cherrie, T.J. Mitchell, W.R. Fright, B.C. McCallum, T.R. Evans, Reconstruction and representation of 3D objects with radial basis functions, in: E. Fiume (Ed.), Computer Graphics Proceedings (Proceedings of SIGGRAPH), Annual Conference Series, ACM Press, New York, 2001, pp. 67–76.

[41] D.E. Kramer, A.A. Volinsky, N.R. Moody, W.W. Gerberich, Substrate effects on indentation plastic zone development in thin soft films, J. Mater. Res. 16 (2001) 3150–3157.

[42] R. Mulford, R.J. Asaro, R.J. Sebring, Spherical indentation of ductile power law materials, J. Mater. Res. 19 (2004) 2641–2649.

[43] L.W. Ma, J.M. Cairney, M. Hoffman, P.R. Munroe, Deformation mechanisms operating during nanoindentation of TiN coatings on steel substrates, Surf. Coat. Technol. 192 (2005) 11–18.

[44] ISO/TR 29381: 2008, Metallic Materials – Measurement of Mechanical Properties by an Instrumented Indentation Test – Indentation Tensile Properties, International Organization for Standardization, Geneva, 2008.

[45] G. Bolzon, G. Maier, M. Panico, Material model calibration by indentation, imprint mapping and inverse analysis, Int. J. Solids Struct. 41 (2004) 2957–2975.

[46] G. Bolzon, V. Buljak, G. Maier, B. Miller, Assessment of elastic-plastic material parameters comparatively by three procedures based on indentation test and inverse analysis, Inverse Probl. Sci. Eng. 19 (2011) 815–837.

[47] ISO 6507–1:2005, Metallic Materials – Vickers Hardness Test – Part 1: Test Method, International Organization for Standardization, Geneva, 2005.

[48] ABAQUS/Standard, Theory and User's Manuals, release 6.9, HKS Inc., Pawtucket, RI, USA, 2009.

[49] M. Bocciarelli, G. Bolzon, G. Maier, A constitutive model of metal–ceramic functionally graded material behavior: formulation and parameter identification, Comput. Mater. Sci. 43 (2008) 16–26.

[50] Q.S. Xia, M.C. Boyce, D.M. Parks, A constitutive model for the anisotropic elastic–plastic deformation of paper and paperboard, Int. J. Solids Struct. 39 (2002) 4053–4071.

[51] J. Castro, M.O. Ostoja-Starzewski, Elasto-plasticity of paper, Int. J. Plast. 19 (2003) 2083–2098.

[52] P. Makela, S. Ostlund, Orthotropic elastic–plastic material model for paper materials, Int. J. Solids Struct. 40 (2003) 5599–5620.

[53] A. Harrysson, M. Ristinmaa, Large strain elasto-plastic model of paper and corrugated board, Int. J. Solids Struct. 45 (2008) 3334–3352.

[54] R. Hill, A theory of the yielding and plastic flow of anisotropic materials, Proc. R. Soc. London A 193 (1948) 281–297.

[55] R. De Borst, P.H. Feenstra, Studies in anisotropic plasticity with reference to the Hill criterion, Int. J. Numer. Methods Eng. 29 (1990) 315–336.

[56] ISO 1924-2: 2008, Paper and board – Determination of Tensile Properties – Part 2: Constant Rate of Elongation Method (20 mm/min), International Organization for Standardization, Geneva, 2008.

[57] L.A.A. Beex, R.H.J. Peerlings, An experimental and computational study of laminated paperboard creasing and folding, Int. J. Solids Struct. 46 (2009) 4192–4207.

[58] P.A. Prates, M.C. Oliveira, N.A. Sakharova, J.V. Fernandes, How to combine the parameters of the yield criteria and the hardening law, Key Eng. Mater. 554–557 (2013) 1195–1202.

[59] J.C. Suhling, R.E. Rowlands, M.W. Johnson, D.E. Gunderson, Tensorial strength analysis of paperboard, Exp. Mech. 25 (1985) 75–84.

[60] M. Ageno, M. Bocciolone, G. Bolzon, A. Cigada, G. Maier, E. Zappa, Mechanical characterisation of thin foils by profilometer masurements of inflated membranes, In: Proceedings 12th International Conference on Experimental Mechanics, ICEM12, 2004; Bari, 1–7.